


Review

# Possibility of Phase Transformation of Al<sub>2</sub>O<sub>3</sub> by a Laser: A Review

Tadas Matijošius <sup>1,2</sup>, Juozas Padgurskas <sup>1</sup> and Gedvidas Bikulčius <sup>2,\*</sup>

<sup>1</sup> Faculty of Engineering, Vytautas Magnus University, LT-53362 Kaunas, Lithuania; tadas.matijosius@vdu.lt (T.M.); juozas.padgurskas@vdu.lt (J.P.)

<sup>2</sup> State Research Institute Center for Physical Sciences and Technology, LT-10257 Vilnius, Lithuania

\* Correspondence: gedvidas.bikulcius@ftmc.lt; Tel.: +370-6-071-9561

**Abstract:** Aluminum (Al) components of high quality often require an optimal ratio of lightness and favorable mechanical properties. In order to improve the physical-mechanical properties of Al, an aluminum oxide (Al<sub>2</sub>O<sub>3</sub>) film is usually formed on the surface of Al, which itself is characterized by high strength, hardness, corrosion resistance, and other technical properties. Unfortunately, depending on the conditions, the oxide film may be formed from different crystal phases on the Al surface, which are not always of desirable quality, i.e., the α-Al<sub>2</sub>O<sub>3</sub> phase. The present review demonstrates that the properties of the Al<sub>2</sub>O<sub>3</sub> film may be improved by Al processing with a laser beam according to the scheme: Al (Al alloy) → electrochemical anodizing → treatment with laser irradiation → α-Al<sub>2</sub>O<sub>3</sub>. Both Al substrate and the anodizing electrolyte affect the phase transformation of anodic Al<sub>2</sub>O<sub>3</sub>. Laser irradiation of the Al<sub>2</sub>O<sub>3</sub> surface leads to high heating and cooling rates, which may promote the formation of a highly crystalline α-Al<sub>2</sub>O<sub>3</sub> phase on anodic Al<sub>2</sub>O<sub>3</sub>.

**Keywords:** ceramic coatings; α-Al<sub>2</sub>O<sub>3</sub>; electrochemistry; laser irradiation

## 1. Introduction

Al and its alloys are widely used in various fields, including aviation and high-tech applications [1–3]. The Al surface is always covered with a native oxide layer of 2–3 nm in thickness [4], but a thicker, denser oxide layer is usually needed. Anodizing is often used to protect Al from external influences, which allows the formation of Al<sub>2</sub>O<sub>3</sub> with a thickness of up to 100 μm [5]. Basically, the properties of Al<sub>2</sub>O<sub>3</sub> depend on the phase structure. Al<sub>2</sub>O<sub>3</sub> can have various metastable phase structures, with the most stable being α-Al<sub>2</sub>O<sub>3</sub> [6]. α-Al<sub>2</sub>O<sub>3</sub> can be obtained through several paths. The list of possible transformations of the phase structures of Al oxides and hydroxides is presented in Figure 1.



**Citation:** Matijošius, T.; Padgurskas, J.; Bikulčius, G. Possibility of Phase Transformation of Al<sub>2</sub>O<sub>3</sub> by a Laser: A Review. *Crystals* **2024**, *14*, 415. <https://doi.org/10.3390/cryst14050415>

Academic Editor: Zaoli Zhang

Received: 1 April 2024

Revised: 18 April 2024

Accepted: 27 April 2024

Published: 28 April 2024



**Copyright:** © 2024 by the authors. Licensee MDPI, Basel, Switzerland. This article is an open access article distributed under the terms and conditions of the Creative Commons Attribution (CC BY) license (<https://creativecommons.org/licenses/by/4.0/>).

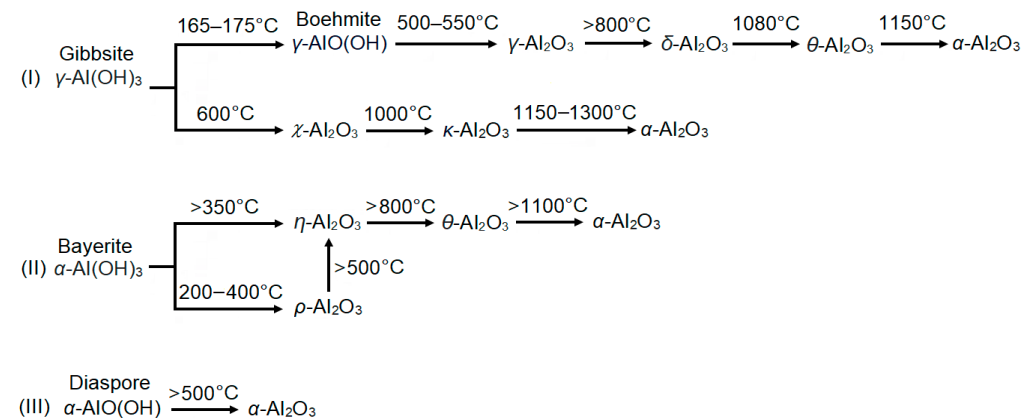


**Figure 1.** Structure transformation of aluminum oxides and aluminum hydroxides.

$\text{Al}_2\text{O}_3$  can exist in the following phases:  $\gamma \rightarrow \delta \rightarrow \theta \rightarrow \alpha$  [7]. The phase structure of  $\text{Al}_2\text{O}_3$  can be formed during its production or by using the calcination method.  $\text{Al}_2\text{O}_3$  is often produced through the Bayer process, beginning with bauxite, which is a naturally occurring ore primarily composed of hydrated aluminum oxides along with various impurities.

Gibbsite ( $\gamma\text{-Al}(\text{OH})_3$ ) is the most common and stable form of  $\text{Al}(\text{OH})_3$  naturally found in bauxite deposits. The transformation of gibbsite to boehmite involves the dehydration and subsequent rearrangement of its crystal structure to the  $\gamma\text{-AlO}(\text{OH})$  phase at  $165^\circ\text{C}$  for 12 h in the steam-assisted crystallization method, and at  $175^\circ\text{C}$  for 12 h in the hydrothermal method [8]. Gibbsite and boehmite are the most commonly used precursors for the preparation of  $\alpha\text{-Al}_2\text{O}_3$ . Boehmite can be transformed into  $\gamma\text{-Al}_2\text{O}_3$  within the temperature range of  $500\text{--}550^\circ\text{C}$  [7]. Temperatures above  $800^\circ\text{C}$  lead to the formation of the  $\delta\text{-Al}_2\text{O}_3$  and  $\theta\text{-Al}_2\text{O}_3$  phases, while the transformation of  $\theta\text{-Al}_2\text{O}_3$  to  $\alpha\text{-Al}_2\text{O}_3$  takes place within the temperature range of  $1050\text{--}1200^\circ\text{C}$  [9]. The densification of  $\text{Al}_2\text{O}_3$  is related to nucleation and grain growth mechanisms and depends on the grain size, heating rate, and chemical composition [10]. Any grain growth process leads to transformation from the  $\theta$  to the  $\alpha$  phase if a critical grain size of  $\sim 20$  nm is reached. However, additional phases of other elements, for example,  $\text{ZrO}_2$  nanoparticles, may inhibit the formation of  $\alpha\text{-Al}_2\text{O}_3$  at temperatures above  $1000^\circ\text{C}$ .

On the other hand, gibbsite can be directly transformed into  $\alpha\text{-Al}_2\text{O}_3$ , bypassing the intermediate  $\chi\text{-Al}_2\text{O}_3$  and  $\kappa\text{-Al}_2\text{O}_3$  phases [11]. The shape and size of  $\text{Al}_2\text{O}_3$  particles affect the phase transformation significantly. Particles larger than 40 nm must undergo the  $\chi\text{-Al}_2\text{O}_3$  to  $\alpha\text{-Al}_2\text{O}_3$  transition via the  $\kappa\text{-Al}_2\text{O}_3$  phase. In contrast, particles smaller than 40 nm may be directly transformed to  $\alpha\text{-Al}_2\text{O}_3$  without passing through the  $\kappa\text{-Al}_2\text{O}_3$  phase at a temperature of  $1050^\circ\text{C}$ , although initial crystal growth is necessary to achieve this size.

The transformation path of bayerite ( $\alpha\text{-Al}(\text{OH})_3$ ) is possible through  $\rho\text{-Al}_2\text{O}_3$ ,  $\eta\text{-Al}_2\text{O}_3$  and  $\theta\text{-Al}_2\text{O}_3$  phases. Due to its instability, bayerite transforms to  $\eta\text{-Al}_2\text{O}_3$  at temperatures higher than  $350^\circ\text{C}$  [12], and is characterized by a higher surface area, acidity, and level of activity when compared to  $\gamma\text{-Al}_2\text{O}_3$  [13]. On the other hand, the  $\eta\text{-Al}_2\text{O}_3$  phase may be obtained via the structural transformation of the  $\rho\text{-Al}_2\text{O}_3$  phase. The dehydration of bayerite leads to the formation of the  $\rho\text{-Al}_2\text{O}_3$  phase at  $200\text{--}400^\circ\text{C}$  under reduced pressure and a slow heating rate [14].  $\rho\text{-Al}_2\text{O}_3$  may be transformed into crystalline  $\alpha\text{-Al}_2\text{O}_3$  via the transitional  $\eta\text{-Al}_2\text{O}_3$  and  $\theta\text{-Al}_2\text{O}_3$  phases, which require thermal treatment at temperatures above  $500^\circ\text{C}$  and  $800^\circ\text{C}$ , respectively [15]. Temperatures above  $1100^\circ\text{C}$  are required to obtain the  $\alpha\text{-Al}_2\text{O}_3$  phase.

Diaspore is known as  $\alpha\text{-AlO}(\text{OH})$  and it shares the same chemical formula as boehmite, but differs in its crystal structure. Along with boehmite and gibbsite, diaspore is one of the main constituents of bauxite, the main raw material used to obtain Al via the Bayer process. Diaspore is stable at temperatures lower than  $380^\circ\text{C}$  [16]. However, it may be converted directly to  $\alpha\text{-Al}_2\text{O}_3$  when heated to above  $500^\circ\text{C}$  [15,17]. Transformations of  $\alpha\text{-Al}_2\text{O}_3$  occur at relatively high temperatures, usually above  $1000^\circ\text{C}$ . In this case, calcined diaspore results in the formation of the  $\alpha\text{-Al}_2\text{O}_3$  phase at temperatures as low as  $600^\circ\text{C}$ .  $\alpha\text{-Al}_2\text{O}_3$  is the most stable  $\text{Al}_2\text{O}_3$  phase and exhibits the same structure as naturally occurring corundum.

In practice,  $\gamma\text{-Al}_2\text{O}_3$  and  $\alpha\text{-Al}_2\text{O}_3$  are the two most popular  $\text{Al}_2\text{O}_3$  phase structures. Since  $\gamma\text{-Al}_2\text{O}_3$  has a large surface area ( $300\text{--}350\text{ m}^2/\text{g}$ ), it is mostly used in catalysis [18]. Meanwhile,  $\alpha\text{-Al}_2\text{O}_3$  is characterized by high hardness (up to 2000 Vickers hardness) and is successfully applied in antifrictional surfaces [19].

In order to improve the functional properties of anodized Al, it is very important to find a method that allows one to enhance the physical-mechanical properties of the anodic layer. It is known that a thin amorphous Si layer can be formed after treating the crystalline Si surface with a nanosecond laser beam [20]. During a nanosecond pulse (about 20 ns), several stages of material transformation are passed: melting, evaporation, and solidification. Since laser treatment of the material allows modification of its phase composition, this

method can be used to treat the  $\text{Al}_2\text{O}_3$  anodic layer with a laser beam, which can ensure the formation of the  $\alpha\text{-Al}_2\text{O}_3$  phase without damaging the Al substrate itself.

The aim of this review is to present different methods for  $\text{Al}_2\text{O}_3$  formation leading to a high crystalline  $\alpha\text{-Al}_2\text{O}_3$  phase. The article summarizes that the  $\alpha\text{-Al}_2\text{O}_3$  phase can be formed by calcination through several different phase structures, or directly by laser irradiation. The importance of heating and cooling rates in  $\text{Al}_2\text{O}_3$  phase transformation is highlighted.

## 2. Dependence of the $\text{Al}_2\text{O}_3$ Phase on Its Formation Method

There are many known  $\text{Al}_2\text{O}_3$  formation methods, including PVD (physical vapor deposition), CVD (chemical vapor deposition), sol-gel, the electrochemical method, PEO (plasma electrolytic oxidation), and laser ablation (Table 1).

**Table 1.** Methods of  $\text{Al}_2\text{O}_3$  formation.

Method	The Phase Structure		Reference
	As Received	After Calcination	
PVD	$\alpha\text{-Al}_2\text{O}_3$	N/A *	[21]
	$\gamma\text{-Al}_2\text{O}_3$	N/A *	[22]
CVD	$\alpha\text{-Al}_2\text{O}_3$	N/A *	[23,24]
Thermal spraying	$\gamma\text{-Al}_2\text{O}_3$ and $\alpha\text{-Al}_2\text{O}_3$	N/A *	[25,26]
Sol-gel	N/A *	$\theta\text{-Al}_2\text{O}_3$ and $\eta\text{-Al}_2\text{O}_3$ at 800 °C; $\alpha\text{-Al}_2\text{O}_3$ at 1200 °C	[27]
	Amorphous $\text{Al}_2\text{O}_3$	$\gamma\text{-Al}_2\text{O}_3$ at 857–1029 °C; $\alpha\text{-Al}_2\text{O}_3$ at 1114–1200 °C	[28]
	N/A *	amorphous $\text{Al}_2\text{O}_3$ at 500–700 °C	[29]
	$\text{AlO}(\text{OH})$ and $\text{Al}(\text{OH})_3$	$\gamma\text{-Al}_2\text{O}_3$ at 415–425 °C	[30]
$\text{H}_2\text{SO}_4$ acid	Amorphous $\text{Al}_2\text{O}_3$	Amorphous $\text{Al}_2\text{O}_3$ to 800 °C; $\gamma\text{-Al}_2\text{O}_3$ at 850–900 °C; $\gamma\text{-Al}_2\text{O}_3$ and $\alpha\text{-Al}_2\text{O}_3$ at 950–1000 °C; $\alpha\text{-Al}_2\text{O}_3$ over 1000 °C	[31]
	$\alpha\text{-Al}_2\text{O}_3$ , $\gamma\text{-Al}_2\text{O}_3$ , and amorphous $\text{Al}_2\text{O}_3$	N/A *	[32]
Oxalic acid	Boehmite, gibbsite, and $\theta\text{-Al}_2\text{O}_3$	$\theta\text{-Al}_2\text{O}_3$ at 500 °C	[33]
	Amorphous $\text{Al}_2\text{O}_3$	$\gamma\text{-Al}_2\text{O}_3$ and $\theta\text{-Al}_2\text{O}_3$ at 750 °C; $\alpha\text{-Al}_2\text{O}_3$ at 1150 °C	[34]
Selenic acid	Amorphous $\text{Al}_2\text{O}_3$	$\gamma\text{-Al}_2\text{O}_3$ at 803 °C; $\alpha\text{-Al}_2\text{O}_3$ at 1153 °C	[35]
Phytic acid	$\alpha\text{-Al}_2\text{O}_3$	N/A *	[36]
$\text{H}_3\text{PO}_4$ and acetic acid	$\gamma\text{-Al}_2\text{O}_3$	N/A *	[37]
$\text{H}_3\text{PO}_4$ and oxalic acid	Amorphous $\text{Al}_2\text{O}_3$	N/A *	[38]
PEO	$\gamma\text{-Al}_2\text{O}_3$ ; $\gamma\text{-Al}_2\text{O}_3$ , and $\alpha\text{-Al}_2\text{O}_3$	N/A *	[39]
	$\gamma\text{-Al}_2\text{O}_3$ and $\alpha\text{-Al}_2\text{O}_3$	N/A *	[40]
Laser ablation	$\gamma\text{-Al}_2\text{O}_3$ ; $\gamma\text{-Al}_2\text{O}_3$ and $\alpha\text{-Al}_2\text{O}_3$	N/A *	[41]
Laser texturing	$\alpha\text{-Al}_2\text{O}_3$	N/A *	[42]
Laser texturing and PEO	$\gamma\text{-Al}_2\text{O}_3$ and $\alpha\text{-Al}_2\text{O}_3$	N/A *	[43]
Laser-assisted CVD	$\alpha\text{-Al}_2\text{O}_3$	N/A *	[44,45]

\* N/A not applicable.

### 2.1. PVD Method

PVD is a technique for thin layer deposition of a material on a substrate surface in vacuum conditions. The formation of  $\text{Al}_2\text{O}_3$  by the PVD method is usually carried out at

low temperatures, which results in amorphous films [46]. Crystalline  $\text{Al}_2\text{O}_3$  can only be obtained at elevated temperatures. For example, Cheng et al. [21] succeeded in obtaining an aluminum oxide film on Si(100) substrates by radio frequency magnetron sputtering using various targets of Al,  $\alpha\text{-Al}_2\text{O}_3$ , and Al + 15 wt%  $\alpha\text{-Al}_2\text{O}_3$  composite at 550 °C. The results showed that the film deposited from the  $\alpha\text{-Al}_2\text{O}_3$  target was composed of both amorphous  $\text{Al}_2\text{O}_3$  and  $\alpha\text{-Al}_2\text{O}_3$ . Meanwhile, Al + 15 wt%  $\alpha\text{-Al}_2\text{O}_3$  composite resulted in an  $\alpha\text{-Al}_2\text{O}_3$  composite film on Si(100). Elsewhere, bipolar pulsed dual magnetron sputtering was applied to deposit nanocrystalline  $\gamma\text{-Al}_2\text{O}_3$  on TiN-precoated cemented carbide substrates at 700 °C [22]. The deposited coatings demonstrated enhanced wear resistance, with surface hardness exceeding 2000 HV.

### 2.2. CVD Method

CVD is a thin film formation process in which precursor gases chemically react with substrates at elevated temperatures. The temperature of the substrate should be over 1000 °C to obtain  $\alpha\text{-Al}_2\text{O}_3$  phase structures [24]. The films deposited by CVD at 900 °C and 1000 °C were found to be of the  $\theta\text{-Al}_2\text{O}_3$  phase, and those deposited at 1100 °C were found to be  $\alpha\text{-Al}_2\text{O}_3$ . According to thermo-gravimetric analysis, CVD-coated specimens exhibited 18 times greater oxidation resistance compared to uncoated samples. Blittersdorf et al. [23] successfully deposited  $\text{Al}_2\text{O}_3$  on stainless steel with a pure  $\alpha\text{-Al}_2\text{O}_3$  structure at a total pressure of 100 mbar and a substrate temperature of 1050 °C. Overall, CVD stands as a versatile and effective method for thin film deposition, offering control over material composition, surface morphology, crystal structure, film thickness, etc. [47].

### 2.3. Thermal Spraying

Thermal spraying is a coating formation process, wherein materials in either melted or heated form are sprayed onto substrates to enhance surface properties, such as hardness, corrosion resistance, wear resistance, and other technical parameters. Among all ceramic materials,  $\text{Al}_2\text{O}_3$  is one of the most commonly used in thermal spraying technologies due to its hardness and abrasion resistance. Thermal spraying can be performed using various methods, such as flame spraying, plasma spraying, high-velocity oxy-fuel (HVOF) spraying, or arc spraying. Heating temperatures can exceed 10,000 °C when the plasma spraying method is used [48]. Several studies have demonstrated that the spraying of  $\text{Al}_2\text{O}_3$  using standard thermally sprayed techniques usually reduces the content of  $\alpha\text{-Al}_2\text{O}_3$ , due to its transformation to the  $\gamma\text{-Al}_2\text{O}_3$  phase [49,50]. On the other hand, the phase transformation of  $\alpha\text{-Al}_2\text{O}_3$  to  $\gamma\text{-Al}_2\text{O}_3$  may be significantly reduced by 8.7% using plasma-sprayed  $\text{Al}_2\text{O}_3$  coatings doped with 13 wt%  $\text{TiO}_2$  [25]. Michalak et al. [26] demonstrated that high velocity oxygen fuel spraying and plasma spraying using  $\text{Al}_2\text{O}_3$  aqueous suspensions resulted in  $\alpha$ -phase rich  $\text{Al}_2\text{O}_3$  coatings of up to 47 vol% and 62 vol%, respectively. Suspension-sprayed  $\text{Al}_2\text{O}_3$  coatings showed much higher wear resistance when compared to that of the coatings obtained by conventional thermal spraying methods.

### 2.4. Sol-Gel Method

The sol-gel method is a wet chemical process used to produce oxide-based materials from small molecules, typically metal alkoxides. This method is attractive because it allows the synthesis of materials at low temperatures [51]. For example, Shojaie-Bahaabad et al. [27] and Wang et al. [28] prepared alumina powders via sol-gel precipitation in ethanol followed by washing-drying treatment and calcination. They demonstrated that the obtained alumina powders had an amorphous phase. The  $\gamma\text{-Al}_2\text{O}_3$  and  $\alpha\text{-Al}_2\text{O}_3$  phases were formed only after heat treatment at temperatures from 857 °C to 1029 °C and from 1114 °C to 1200 °C, respectively.

Hu et al. [29] produced crack-free amorphous structured  $\text{Al}_2\text{O}_3$  films from Al isopropoxide using the spin coating method and then calcined them at 500 °C for 3 h. During the formation of  $\text{Al}_2\text{O}_3$  powder by the sol-gel method, boehmite ( $\text{AlOOH}$ ) was obtained at 20 °C, and  $\gamma\text{-Al}_2\text{O}_3$  was formed after calcination at 600 °C [30]. Attention should be drawn

to the fact that the structure of  $\text{Al}_2\text{O}_3$  derivatives obtained by the sol-gel method may be different after calcination (Table 1), depending on the reagents used for specific cases.

### 2.5. Electrochemical Method

One of the most widely accepted  $\text{Al}_2\text{O}_3$  formation techniques is based on the electrochemical method [52]. Electrochemical oxidation (anodizing) is an electrolytic passivation process that contributes to an increase in the thickness of the natural oxide layer on the metal surface and enhances surface hardness, corrosion resistance, and other technical features [53]. Non-porous barrier oxide coatings are usually formed in neutral or alkaline electrolytes, while porous coatings are produced in acidic electrolytes. This method relies on two competing processes: the formation of an oxide coating, and its chemical dissolution. Anodizing in acidic electrolytes produces porous coatings with a thickness of up to 100  $\mu\text{m}$  or more, ending with a thin non-porous barrier layer next to the metal surface [5,54]. Anodic coatings are composed mainly of amorphous  $\text{Al}_2\text{O}_3$ , but a crystalline  $\gamma\text{-Al}_2\text{O}_3$  phase with a grain size of about 20 nm may be formed by increasing anodizing voltage up to 100 V [55]. Sulfates, oxalates, hydroxides, and other compounds have also been found during anodizing, but on a much lower scale. Usually, porous anodic alumina can incorporate up to 14 wt% sulfates, up to 8 wt% phosphates, and up to 3 wt% oxalates [56].

The phase transformation of amorphous  $\text{Al}_2\text{O}_3$  to crystalline  $\alpha\text{-Al}_2\text{O}_3$  often requires heat treatment at elevated temperatures [57]. In one study, anodic aluminum oxide (AAO) films were formed in a 15%  $\text{H}_2\text{SO}_4$  solution by the anodizing method, and the prepared AAO films were heat-treated in the temperature range of 25–1000  $^\circ\text{C}$ . The phase structure of the  $\text{Al}_2\text{O}_3$  was amorphous and remained unchanged when heated to 800  $^\circ\text{C}$ . The  $\gamma\text{-Al}_2\text{O}_3$  phase was formed after calcination of  $\text{Al}_2\text{O}_3$  at 950  $^\circ\text{C}$ . As the calcination temperature was increased, AAO represented a mixture of  $\gamma\text{-Al}_2\text{O}_3$  and  $\alpha\text{-Al}_2\text{O}_3$  phases. Once a temperature of 1000  $^\circ\text{C}$  was reached, AAO totally transformed into the  $\alpha\text{-Al}_2\text{O}_3$  phase [31].

Tian et al. [33] anodized Al alloys of 99.999% purity in an oxalic acid electrolyte using the two-step anodizing method. Before anodizing, the samples were annealed at 500  $^\circ\text{C}$  for 2 h in a nitrogen environment. X-ray diffraction (XRD) data showed that the  $\text{Al}_2\text{O}_3$  consisted of a mixture of amorphous and  $\theta\text{-Al}_2\text{O}_3$  phases. Annealing at 500  $^\circ\text{C}$  resulted in the predominance of  $\theta\text{-Al}_2\text{O}_3$ . Meanwhile, Roslyakov et al. [34] anodized Al alloys of 99.99% purity in oxalic acid, without annealing the samples before anodizing. In this case, the obtained  $\text{Al}_2\text{O}_3$  phase was amorphous. Different  $\text{Al}_2\text{O}_3$  phases were detected after calcination at various temperatures:  $\gamma\text{-Al}_2\text{O}_3$  and  $\theta\text{-Al}_2\text{O}_3$  at 750  $^\circ\text{C}$ , and  $\alpha\text{-Al}_2\text{O}_3$  at 1150  $^\circ\text{C}$ .

Roslyakov et al. [35] anodized 99.99 wt% Al alloy without preheating in a selenic acid electrolyte. The obtained  $\text{Al}_2\text{O}_3$  was characterized by amorphousness. It was found that  $\text{Al}_2\text{O}_3$  transformed into the  $\gamma\text{-Al}_2\text{O}_3$  and  $\alpha\text{-Al}_2\text{O}_3$  phases after calcination at temperatures of 803  $^\circ\text{C}$  and 1153  $^\circ\text{C}$ , respectively.

Kim et al. [36] anodized Al alloy 6060-T6 using a 9.5 M phytic acid electrolyte. XRD analysis showed that the predominant  $\alpha\text{-Al}_2\text{O}_3$  phase was formed in this electrolyte, especially when  $\text{Al}_2\text{O}_3$  was grown at temperatures of 0–10  $^\circ\text{C}$ . According to the authors, crystalline  $\alpha\text{-Al}_2\text{O}_3$  ensures high corrosion resistance.

Since the anodizing electrolyte affects the phase composition of the  $\text{Al}_2\text{O}_3$  coating, it is also important to consider the effect of the acid mixture on Al anodizing. Juyana et al. [37] steamed Al samples by melting Al pellets in a vacuum environment at 850  $^\circ\text{C}$  and performed their anodization in a mixture of  $\text{H}_3\text{PO}_4$  and acetic acids, obtaining dominantly  $\gamma\text{-Al}_2\text{O}_3$ . Kao et al. [38] anodized Al samples of 99.98% purity in a mixed solution of  $\text{H}_3\text{PO}_4$  and oxalic acids. The results obtained showed that the formed  $\text{Al}_2\text{O}_3$  film was amorphous. Interestingly, annealing of  $\text{Al}_2\text{O}_3$ , for example, at 600  $^\circ\text{C}$  for 2 h, did not change its phase, and the  $\text{Al}_2\text{O}_3$  remained amorphous.



## 2.6. PEO Method

PEO is an electrochemical surface treatment method used to produce thick, hard, dense, and highly crystalline ceramic coatings on Al, Mg, and Ti alloys. It is clear that during the anodizing of Al, amorphous or  $\gamma$ -Al<sub>2</sub>O<sub>3</sub> phase structures are usually predominant (Table 1). The PEO method was used to produce  $\alpha$ -Al<sub>2</sub>O<sub>3</sub> by directly anodizing the Al substrate without further calcination, which significantly improved the physical-mechanical properties of Al. In other words, PEO is an electrochemical surface treatment method used in aqueous electrolytes [58] in which the plasma temperature can vary from 3500 K (3227 °C) to 16,000 K (15,727 °C) on the Al surface [59]. Unlike electrochemical anodizing, where acidic electrolytes are most often used, the PEO coating formation method is usually performed in alkaline electrolytes (KOH, Na<sub>2</sub>SiO<sub>3</sub>, Na<sub>3</sub>PO<sub>4</sub>, NaAlO<sub>2</sub>, and Na<sub>2</sub>O·3SiO<sub>2</sub>) with inorganic salts and additives that make PEO electrolytes environmentally friendly. The PEO process is performed at high voltage (up to 700 V), resulting in the formation of electrical micro-discharges caused by the localized dielectric breakdown of the growing oxide coating, which determines the structure, morphology, and phase composition of the coating. The PEO process involves three simultaneous operations: electrochemical reactions, plasma-chemical reactions, and thermo-chemical reactions [60]. PEO coatings typically exhibit a morphological structure characterized by three distinct layers [60,61]. The outer layer, constituting approximately 5% to 30% of the coating thickness, often displays defects such as cracks and pores. It predominantly comprises the  $\gamma$ -Al<sub>2</sub>O<sub>3</sub> phase and exhibits relatively low hardness values, typically from 500 HV to 1000 HV. The intermediate layer, comprising 70% to 95% of the total coating thickness, exhibits a greater density and is composed of both  $\gamma$ -Al<sub>2</sub>O<sub>3</sub> and  $\alpha$ -Al<sub>2</sub>O<sub>3</sub> phases, with a hardness ranging from 900 HV to 2000 HV. The inner layer is amorphous Al<sub>2</sub>O<sub>3</sub> and facilitates strong adhesion to the coating and metal substrate. This method makes it possible to produce hard coatings with a thickness exceeding 100  $\mu$ m [62]. The PEO method can enhance surface hardness to values ranging from 1000 to 1500 HV and improve wear resistance by 3–5 times [63]. Famiyeh and Huang [39] demonstrated that a mixture of  $\gamma$ -Al<sub>2</sub>O<sub>3</sub> and  $\alpha$ -Al<sub>2</sub>O<sub>3</sub> phases is most often characteristic of the Al<sub>2</sub>O<sub>3</sub> coatings obtained by the PEO method. However, the distribution of the  $\alpha$ -Al<sub>2</sub>O<sub>3</sub> and  $\gamma$ -Al<sub>2</sub>O<sub>3</sub> phases in coatings strongly depends on the compositions of the Al substrate and anodizing electrolyte. Notably, during the initial stages of the PEO process (for the first 5 to 10 min), only the  $\gamma$ -Al<sub>2</sub>O<sub>3</sub> phase was observed in the coating. The  $\alpha$ -Al<sub>2</sub>O<sub>3</sub> phase appeared and remained predominant after 30–60 min due to the development of micro-discharges during the PEO process. Similar results have been obtained by other scientists [40].

## 2.7. Laser Ablation and Texturing

In order to create a textured surface, the most suitable method is laser surface texturing. This is a process related to the removal of material (ablation), which enables changes in the properties of the body surface including the tribological characteristics, wettability, roughness, phase structure, etc. [64]. Laser surface texturing has been extensively used in various applications to improve the adhesive bonding of coatings and films [65,66], the wettability of self-cleaning surfaces [67], antibacterial properties for biomedical applications [68,69], anti-reflection properties for solar cells [70], and to reduce adhesion and stiction in micro-electro-mechanical systems [71] and enhance friction and wear resistance in mechanical components like gears [72], seals [73], piston rings [74], cutting tools [75], and implants [76]. The laser ablation method has also found a unique application in cancer treatment [77]. The most essential factor for cancer treatment of a specific organ or tissue is the laser penetration depth, which depends on the laser type and wavelength. For example, CO<sub>2</sub> lasers with a wavelength of 10,600 nm have a low penetration depth and are most suitable for skin cancer treatment. Nd:YAG (1064 nm) and diode (800–970 nm) lasers can penetrate into deeper tissues and are used to treat liver, breast, brain, and other cancers. Overall, laser ablation is a minimally invasive technique that causes local heating of tissues,

with temperatures reaching 100 °C to 1000 °C in a short period of time (~0.1 s), resulting in material loss and tissue removal.

Laser texturing allows the formation of specific design patterns, such as pits, dimples, and grooves, on a variety of engineering materials, including polymers, metals, and ceramics. Based on surface texture fabrication, this method can be divided into three groups: (I) direct laser ablation; (II) direct laser interference patterning; and (III) laser shock peening [72]. Direct laser ablation is the process of removing material by irradiation with a laser beam at high efficiency and controllability, which results in specific surface patterning with sizes ranging from one to several hundred micrometers [78]. Functional periodic microstructures can be created by interference of two or more coherent laser beams using direct laser interference patterning (DLIP). Laser interference is capable of creating texture features with a high resolution and a fabrication speed of 0.1 m<sup>2</sup>/min, leading to structure sizes ranging from 1 μm to 100 μm [72]. Laser shock peening (LSP) is an advanced surface treatment technique based on laser shock-induced plastic deformation without a thermal effect. These shockwaves induce changes in the material microstructure and residual stress distribution, resulting in improved surface hardening, wear resistance, and tribological performance [79,80]. Shukla et al. [81] demonstrated increased net compressive stresses from 104 MPa to 168 MPa using LSP on Al<sub>2</sub>O<sub>3</sub> ceramics. Elsewhere, LSP has resulted in significant compressive residual stresses, which improved the resistance of polycrystalline α-Al<sub>2</sub>O<sub>3</sub> to indentation cracking [82].

Several studies have been devoted to the role of laser texturing in Al<sub>2</sub>O<sub>3</sub> phase transformation. Jing et al. [42] demonstrated that the texturing of Al<sub>2</sub>O<sub>3</sub> ceramics obtained by the hot-pressing sintering method with a fiber laser of 1064 nm wavelength, 50 ns pulse duration, 20 kHz repetition rate, and 1 mJ pulse resulted in a reduced coefficient of friction from 0.48 to 0.38 under lubricated friction conditions. XRD analysis showed that mainly the α-Al<sub>2</sub>O<sub>3</sub> phase was formed on the ceramic surface. Ismail et al. [41] formed Al<sub>2</sub>O<sub>3</sub> nanoparticles by laser ablation of an Al target in ethanol. XRD studies showed that the phase composition of the Al<sub>2</sub>O<sub>3</sub> nanoparticles depended on the 532 nm laser fluence. The γ-Al<sub>2</sub>O<sub>3</sub> phase was formed at 3.5 J/cm<sup>2</sup>/pulse, while γ-Al<sub>2</sub>O<sub>3</sub> and α-Al<sub>2</sub>O<sub>3</sub> were obtained at 5.3 J/cm<sup>2</sup>/pulse.

### 2.8. Laser Texturing and PEO

Crystalline Al<sub>2</sub>O<sub>3</sub> can also be obtained using combined methods for Al surface preparation. Li et al. [43] demonstrated that the friction and corrosion resistance of Al alloy 6061 can be enhanced by formation of a protective coating using two processes: laser texturing and PEO. According to the data of XRD studies, laser texturing with a picosecond pulse laser followed by PEO has resulted in coatings with α-Al<sub>2</sub>O<sub>3</sub> and γ-Al<sub>2</sub>O<sub>3</sub> phases.

### 2.9. Laser-Assisted CVD

Ito et al. [44] presented a method based on CVD in combination with an Nd:YAG laser of 1064 nm wavelength to form crystalline Al<sub>2</sub>O<sub>3</sub> coatings. α-Al<sub>2</sub>O<sub>3</sub> coatings were obtained in the region at precursor vaporization temperatures above 150 °C (423 K) and deposition temperatures above 827 °C (1100 K), at a total chamber pressure of 0.93 kPa. The orientation and texture of the α-Al<sub>2</sub>O<sub>3</sub> film also depended on the deposition conditions, such as temperature and pressure. Elsewhere, the laser-assisted CVD method using a laser beam of 808 nm wavelength resulted in coatings consisting of the α-Al<sub>2</sub>O<sub>3</sub> phase on polycrystalline AlN substrates at deposition temperatures of 1100–1182 °C (1373–1455 K) [45].

## 3. Al<sub>2</sub>O<sub>3</sub> Structure Transformation Depending on Heating and Cooling Rates

In order to form α-Al<sub>2</sub>O<sub>3</sub>, the simplest method is to calcinate the original Al<sub>2</sub>O<sub>3</sub> at a certain temperature. However, it has been observed that Al<sub>2</sub>O<sub>3</sub> phase transformation depends on both heating and cooling rates. Lamouri et al. [7] showed that γ-Al<sub>2</sub>O<sub>3</sub> can be transformed into the α-Al<sub>2</sub>O<sub>3</sub> phase by increasing the heating temperature from room temperature up to 1200 °C. In addition, they found that the phase transformation of

$\text{Al}_2\text{O}_3$  depended on the heating rate, as determined by differential thermal analysis and dilatometry. Low heating rates led to a significant reduction in temperature from 1240 °C to 1190 °C, representing a temperature difference of 50 °C for  $\alpha\text{-Al}_2\text{O}_3$  formation. The optimal heating rate was equal to 5 °C/min, leading to high relative density, low residual porosity, and a homogeneous microstructure.

Sathyaseelan et al. [83] demonstrated that heating of  $\text{Al}_2\text{O}_3$  powder for 2 h at a heating rate of 20 °C/min lead to the formation of the  $\alpha\text{-Al}_2\text{O}_3$  phase at 900 °C. Meanwhile, Matori et al. [84] demonstrated that the  $\alpha\text{-Al}_2\text{O}_3$  phase is formed only at 1200 °C by heating of  $\text{Al}_2(\text{SO}_4)_3 \cdot 18\text{H}_2\text{O}$  at 400–1400 °C for 3 h with heating and cooling rates of 10 °C/min. Palmero et al. [85] investigated the phase transformation of 47 nm particles of the  $\delta\text{-Al}_2\text{O}_3$  and  $\gamma\text{-Al}_2\text{O}_3$  phases to  $\alpha\text{-Al}_2\text{O}_3$  by increasing the heating temperature at a rate of 1 °C/min or 10 °C/min and cooling the samples at a rate of 20 °C/min. They found that a longer heating time (i.e., slower heating rate of 1000–1135 °C) resulted in more efficient formation of  $\alpha$ -phases. Such material heating and cooling rates can be obtained using a standard heating furnace (Figure 2). This is a relatively slow calcination method.

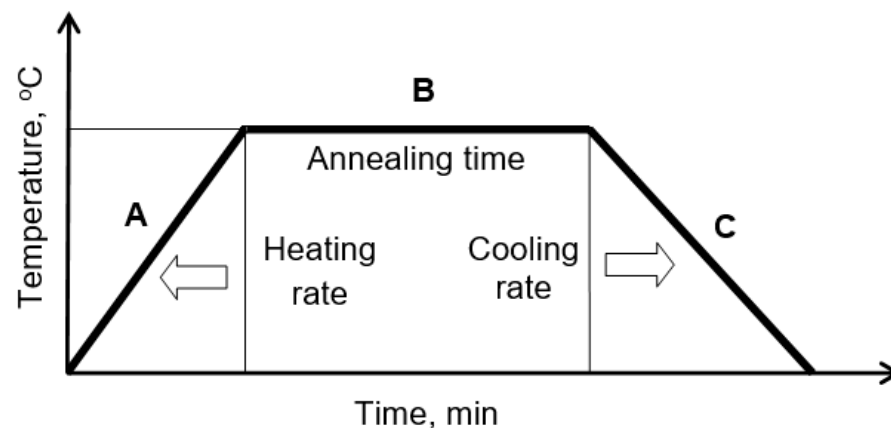


**Figure 2.** The annealing of  $\text{Al}_2\text{O}_3$  in the furnace: (A) heating, (B) annealing, and (C) cooling.

Mahat et al. [86] studied the influence of heating temperature on the phase state of  $\text{Al}_2\text{O}_3$  particles. According to the XRD method, the  $\eta\text{-Al}_2\text{O}_3$  and  $\alpha\text{-Al}_2\text{O}_3$  phases were formed after the heating of  $\text{Al}_2\text{O}_3$  particles for 48 h at 800 °C and 1000 °C, respectively.

Since heating and cooling rates influence the phase structure of  $\text{Al}_2\text{O}_3$ , it would be of interest to examine what effects rapid heating and cooling would have on the phase structure of the material. Application of a laser beam would be the most appropriate method for such an examination. Laser application for polishing [87], texturing [88], and shock peening [89] results in material structural changes (formation of crystallites, phase transformation, etc.), which inevitably affects the physical-mechanical properties of the material. Therefore, it is important to understand the possible effects of laser beam interaction with the material. Nanosecond (ns), picosecond (ps), and femtosecond (fs) lasers can increase surface temperatures up to 2000 °C [90,91], and even further up to 10,000 °C [92]. The shorter the duration of the laser pulse, the slighter the effect on surrounding temperature [93].

Farshidianfar et al. [94] studied the changes in the microstructure of stainless steel 316L powder melted on an AISI1030 carbon steel substrate with dependence on the solidification and cooling rates. They showed that the cooling rate directly affected the formation and growth of the phase structure, grain boundaries, and grain size. The grain diameter decreased with the increasing cooling rate. The cooling time typically varied from 22 °C/s to 764 °C/s, but in some cases it was possible to reach cooling rates of  $7.93 \times 10^6$  °C/s [91].

The influence of the fast heating and cooling of polymers was studied across a very wide range of cooling and heating rates ( $10^{-2}$  to  $10^6$  K/s) using the fast scanning calorimetry method, and it was found that high heating rates affected the kinetics of crystallization [95]. Lee et al. [96] studied  $\text{Cu}_{50}\text{Zr}_{50}$  metallic glass thin films under a wide range of temperature



variations (13 K/s to 21,000 K/s) and demonstrated that the critical rate to avoid crystallization is much higher during heating than that during cooling. Therefore, the treatment of materials with laser irradiation allows maximum rapid heating and cooling rates (Figure 3).

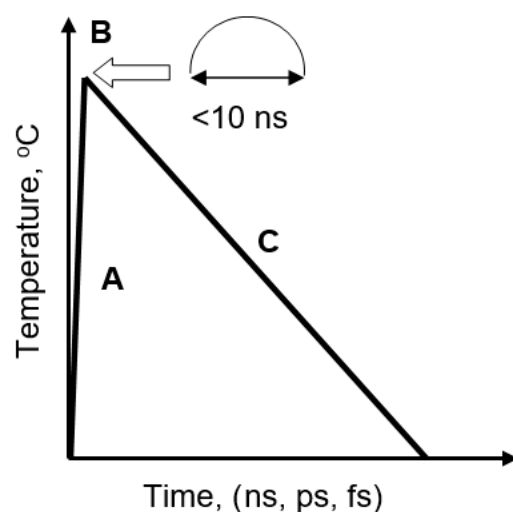


**Figure 3.** The heating-cooling profile of  $\text{Al}_2\text{O}_3$  treatment by laser irradiation: (A) heating, (B) annealing, and (C) cooling.

Laser treatment can have the opposite effect on phase transformation. Ibrahim and Hung [97] investigated 5 mm thick  $\text{Al}_2\text{O}_3$  coatings with 13 wt%  $\text{TiO}_2$  on mild steel. XRD studies showed that the powdered  $\alpha\text{-Al}_2\text{O}_3$  phase transformed into the  $\gamma\text{-Al}_2\text{O}_3$  phase only if the plasma spraying method was applied, whereas surface treatment with a laser possessing a wavelength of 248 nm and pulse duration of 24 ns led to a reduction in the  $\gamma$  phase of  $\text{Al}_2\text{O}_3$ . This effect indicated that a very high cooling rate was achieved using an ns pulsed laser, which suppressed the transformation of  $\gamma\text{-Al}_2\text{O}_3$  to  $\alpha\text{-Al}_2\text{O}_3$ . In our opinion, such  $\text{Al}_2\text{O}_3$  transformations in both the plasma sprayed and laser treatment stages are related to short-term heating of the oxide and short-term cooling, i.e., the time required for the formation of the corresponding phase is insufficient, as opposed to  $\text{Al}_2\text{O}_3$  being annealed in a furnace. Moriya et al. [98] demonstrated that it is possible to achieve phase transformation of alumina sprayed coatings from  $\gamma\text{-Al}_2\text{O}_3$  to  $\alpha\text{-Al}_2\text{O}_3$  by using laser irradiation of 1064 nm wavelength and reducing laser scan speed, which is associated with a lower cooling rate. Phase transformation into  $\alpha\text{-Al}_2\text{O}_3$  led to the formation of a dense pore-free surface microstructure with a reduced crack number, which was expected to improve the corrosion and wear resistance of the coatings. Nevertheless, current knowledge of the variations in the phase structure of anodic  $\text{Al}_2\text{O}_3$  with laser beam treatment is still insufficient. This topic remains debatable.

#### 4. Conclusions

The data analysis suggests that  $\text{Al}_2\text{O}_3$  can be transformed into high crystalline  $\alpha\text{-Al}_2\text{O}_3$  through several heating stages at high temperatures, or directly by laser irradiation. Several key points should be taken into account in order to improve the crystallinity of anodic  $\text{Al}_2\text{O}_3$ .

1. The phase of anodic  $\text{Al}_2\text{O}_3$  depends on its formation method and electrolyte composition.
2. The nature of the Al substrate may affect the phase composition of anodic  $\text{Al}_2\text{O}_3$ .
3. The phase of anodic  $\text{Al}_2\text{O}_3$  is determined not only by the annealing temperature, but also by the heating and cooling rates.
4. Annealing of pure Al substrate before anodizing has no pronounced impact on the phase structure of anodic  $\text{Al}_2\text{O}_3$ .

5. High heating and cooling rates influence the formation of the  $\alpha$ -Al<sub>2</sub>O<sub>3</sub> phase when using laser irradiation. Therefore, laser treatment might be beneficial for the formation of a highly crystalline  $\alpha$  phase on anodic Al<sub>2</sub>O<sub>3</sub> in a very thin surface layer.

**Author Contributions:** Conceptualization, G.B.; formal analysis, G.B. and T.M.; investigation, G.B. and T.M.; writing—original draft preparation, G.B. and T.M.; writing—review and editing, G.B., J.P. and T.M.; visualization, G.B. and T.M.; supervision, G.B.; project administration, J.P.; funding acquisition, T.M. All authors have read and agreed to the published version of the manuscript.

**Funding:** This project has received funding from the Research Council of Lithuania (LMTLT), agreement No S-PD-22-106.

**Data Availability Statement:** No new data were created or analyzed in this study. Data sharing is not applicable to this article.

**Conflicts of Interest:** The authors declare no conflicts of interest.

## References

1. Heinz, A.; Haszler, A.; Keidel, C.; Moldenhauer, S.; Benedictus, R.; Miller, W.S. Recent development in aluminium alloys for aerospace applications. *Mater. Sci. Eng. A* **2000**, *280*, 102–107. [[CrossRef](#)]
2. Williams, J.C.; Starke, E.A., Jr. Progress in structural materials for aerospace systems. *Acta Mater.* **2003**, *51*, 5775–5799. [[CrossRef](#)]
3. Xu, W.; Luo, Y.; Zhang, W.; Fu, M. Comparative study on local and global mechanical properties of bobbin tool and conventional friction stir welded 7085-T7452 aluminum thick plate. *J. Mater. Sci. Technol.* **2018**, *34*, 173–184. [[CrossRef](#)]
4. Jeong, H.Y.; Lee, J.Y.; Choi, S.Y.; Kim, J.W. Microscopic origin of bipolar resistive switching of nanoscale titanium oxide thin films. *Appl. Phys. Lett.* **2009**, *95*, 162108. [[CrossRef](#)]
5. Zaraska, L.; Sulka, G.D.; Jaskuła, M. Anodic alumina membranes with defined pore diameters and thicknesses obtained by adjusting the anodizing duration and pore opening/widening time. *J. Solid State Electrochem.* **2011**, *15*, 2427–2436. [[CrossRef](#)]
6. Shirai, T.; Watanabe, H.; Fuji, M.; Takahashi, M. Structural properties and surface characteristics on aluminum oxide powders. *Annu. Rep. Ceram. Res. Lab. Nagoya Inst. Technol.* **2009**, *9*, 23–31.
7. Lamouri, S.; Hamidouche, M.; Bouaouadja, N.; Belhouche, H.; Garnier, V.; Fantozzi, G.; Trelkat, J.F. Control of the  $\gamma$ -alumina to  $\alpha$ -alumina phase transformation for an optimized alumina densification. *Bol. Soc. Esp. Ceram. Vidr.* **2017**, *56*, 47–54. [[CrossRef](#)]
8. Chen, B.; Xu, X.; Chen, X.; Kong, L.; Chen, D. Transformation behavior of gibbsite to boehmite by steam-assisted synthesis. *J. Solid State Chem.* **2018**, *265*, 237–243. [[CrossRef](#)]
9. Kovarik, L.; Bowden, M.; Szanyi, J. High temperature transition aluminas in  $\delta$ -Al<sub>2</sub>O<sub>3</sub>/ $\theta$ -Al<sub>2</sub>O<sub>3</sub> stability range. *J. Catal.* **2021**, *393*, 357–368. [[CrossRef](#)]
10. Koltsov, I.; Smalc-Koziorowska, J.; Przeźniak-Welenc, M.; Małysa, M.; Kimmel, G.; McGlynn, J.; Ganin, A.; Stelmakh, S. Mechanism of reduced sintering temperature of Al<sub>2</sub>O<sub>3</sub>-ZrO<sub>2</sub> nanocomposites obtained by microwave hydrothermal synthesis. *Materials* **2018**, *11*, 829. [[CrossRef](#)]
11. Chang, P.L.; Wu, Y.C.; Lai, S.J.; Yen, F.S. Size effects on  $\chi$ -to  $\alpha$ -Al<sub>2</sub>O<sub>3</sub> phase transformation. *J. Eur. Ceram. Soc.* **2009**, *29*, 3341–3348. [[CrossRef](#)]
12. Isfahani, T.; Javadpour, J.; Khavandi, A. Formation mechanism and phase transformations in mechanochemically prepared Al<sub>2</sub>O<sub>3</sub>-40wt% ZrO<sub>2</sub> nanocomposite powder. *Compos. Interfaces* **2019**, *26*, 887–904. [[CrossRef](#)]
13. Vaidya, S.D.; Thakkar, N.V. Effect of temperature, pH and ageing time on hydration of rho alumina by studying phase composition and surface properties of transition alumina obtained after thermal dehydration. *Mater. Lett.* **2001**, *51*, 295–300. [[CrossRef](#)]
14. Sato, T. Preparation of Rho Alumina. *Shigen Sozai* **2004**, *120*, 197–201. [[CrossRef](#)]
15. Chandran, C.V.; Kirschhock, C.E.; Radhakrishnan, S.; Taulelle, F.; Martens, J.A.; Breynaert, E. Alumina: Discriminative analysis using 3D correlation of solid-state NMR parameters. *Chem. Soc. Rev.* **2019**, *48*, 134–156. [[CrossRef](#)]
16. Garcia-Guinea, J.; Correcher, V.; Rubio, J.; Valle-Fuentes, F.J. Effects of preheating on diasporite: Modifications in colour centres, structure and light emission. *J. Phys. Chem. Solids* **2005**, *66*, 1220–1227. [[CrossRef](#)]
17. van Gog, H. First-principles study of dehydration interfaces between diasporite and corundum, gibbsite and boehmite, and boehmite and  $\gamma$ -Al<sub>2</sub>O<sub>3</sub>: Energetic stability, interface charge effects, and dehydration defects. *Appl. Surf. Sci.* **2021**, *541*, 148501. [[CrossRef](#)]
18. Trueba, M.; Trasatti, S.P.  $\gamma$ -Alumina as a support for catalysts: A review of fundamental aspects. *Eur. J. Inorg. Chem.* **2005**, *2005*, 3393–3403. [[CrossRef](#)]
19. Aryasomayajula, A.; Randall, N.X.; Gordon, M.H.; Bhat, D. Tribological and mechanical properties of physical vapor deposited alpha alumina thin film coating. *Thin Solid Films* **2008**, *517*, 819–823. [[CrossRef](#)]
20. Tian, L.; Wang, X. Pulsed laser-induced rapid surface cooling and amorphization. *Jpn. J. Appl. Phys.* **2008**, *47*, 8113. [[CrossRef](#)]
21. Cheng, Y.; Qiu, W.; Zhou, K.; Yang, Y.; Jiao, D.; Liu, Z.; Zhong, X. Low-temperature deposition of  $\alpha$ -Al<sub>2</sub>O<sub>3</sub> film using Al+  $\alpha$ -Al<sub>2</sub>O<sub>3</sub> composite target by radio frequency magnetron sputtering. *Mater. Res. Express* **2019**, *6*, 086412. [[CrossRef](#)]

22. Åstrand, M.; Selinder, T.I.; Fietzke, F.; Klostermann, H. PVD- $\text{Al}_2\text{O}_3$ -coated cemented carbide cutting tools. *Surf. Coat. Technol.* **2004**, *188*, 186–192. [[CrossRef](#)]
23. Blittersdorf, S.; Bahlawane, N.; Kohse-Höinghaus, K.; Atakan, B.; Müller, J. CVD of  $\text{Al}_2\text{O}_3$  thin films using aluminum triisopropoxide. *Chem. Vap. Depos.* **2003**, *9*, 194–198. [[CrossRef](#)]
24. Dhonge, B.P.; Mathews, T.; Kumar, N.; Ajikumar, P.K.; Manna, I.; Dash, S.; Tyagi, A.K. Wear and oxidation resistance of combustion CVD grown alumina films. *Surf. Coat. Technol.* **2012**, *206*, 4574–4579. [[CrossRef](#)]
25. Šuopys, A.; Marcinauskas, L.; Grigaitienė, V.; Kėželis, R.; Aikas, M.; Uscila, R.; Tučkutė, S.; Lelis, M. The effect of heat treatment on the microstructure and phase composition of plasma sprayed  $\text{Al}_2\text{O}_3$  and  $\text{Al}_2\text{O}_3$ - $\text{TiO}_2$  coatings for applications in biomass firing plants. *Coatings* **2021**, *11*, 1289. [[CrossRef](#)]
26. Michalak, M.; Latka, L.; Sokolowski, P.; Toma, F.L.; Myalska, H.; Denoirjean, A.; Ageorges, H. Microstructural, mechanical and tribological properties of finely grained  $\text{Al}_2\text{O}_3$  coatings obtained by SPS and S-HVOF methods. *Surf. Coat. Technol.* **2020**, *404*, 126463. [[CrossRef](#)]
27. Shojaie-Bahaabad, M.; Taheri-Nassaj, E. Economical synthesis of nano alumina powder using an aqueous sol-gel method. *Mater. Lett.* **2008**, *62*, 3364–3366. [[CrossRef](#)]
28. Wang, S.; Li, X.; Wang, S.; Li, Y.; Zhai, Y. Synthesis of  $\gamma$ -alumina via precipitation in ethanol. *Mater. Lett.* **2008**, *62*, 3552–3554. [[CrossRef](#)]
29. Hu, B.; Jia, E.; Du, B.; Yin, Y. A new sol-gel route to prepare dense  $\text{Al}_2\text{O}_3$  thin films. *Ceram. Int.* **2016**, *42*, 16867–16871. [[CrossRef](#)]
30. Rutkowska, I.; Marchewka, J.; Jeleń, P.; Odziomek, M.; Korpyś, M.; Paczkowska, J.; Sitarz, M. Chemical and structural characterization of amorphous and crystalline alumina obtained by alternative sol-gel preparation routes. *Materials* **2021**, *14*, 1761. [[CrossRef](#)]
31. Liu, X.Z.; Yan, X.H.; Wang, G.; Liu, X.Z.; Chen, J.; Zhu, Y.C. Preparation and Effect of Heat Treatment Temperature on the Crystal Phase of Anodic Aluminum Oxide Films. *Appl. Mech. Mater.* **2014**, *577*, 11–14. [[CrossRef](#)]
32. Benea, L.; Simionescu-Bogatu, N.; Chiriac, R. Electrochemically obtained  $\text{Al}_2\text{O}_3$  nanoporous layers with increased anticorrosive properties of aluminum alloy. *J. Mater. Res. Technol.* **2022**, *17*, 2636–2647. [[CrossRef](#)]
33. Tian, Y.M.; Xu, M.X.; Liu, X.Z.; Ge, L.; Zhang, P. Microstructure Control and Phase Structure Study of Porous Alumina Membrane. *Key Eng. Mater.* **2007**, *336*, 2232–2234. [[CrossRef](#)]
34. Roslyakov, I.V.; Kolesnik, I.V.; Levin, E.E.; Katorova, N.S.; Pestrikov, P.P.; Kardash, T.Y.; Solovyov, L.A.; Napolskii, K.S. Annealing induced structural and phase transitions in anodic aluminum oxide prepared in oxalic acid electrolyte. *Surf. Coat. Technol.* **2020**, *381*, 125159. [[CrossRef](#)]
35. Roslyakov, I.V.; Shirin, N.A.; Evdokimov, P.V.; Berekchiian, M.V.; Simonenko, N.P.; Lyskov, N.V.; Napolskii, K.S. High-temperature annealing of porous anodic aluminium oxide prepared in selenic acid electrolyte. *Surf. Coat. Technol.* **2022**, *433*, 128080. [[CrossRef](#)]
36. Kim, M.; Choi, E.; So, J.; Shin, J.S.; Chung, C.W.; Maeng, S.J.; Yun, J.Y. Improvement of corrosion properties of plasma in an aluminum alloy 6061-T6 by phytic acid anodization temperature. *J. Mater. Res. Technol.* **2021**, *11*, 219–226. [[CrossRef](#)]
37. Juyana, A.W.; Derman, M.N.B. Characterization of porous anodic aluminium oxide film on aluminium templates formed in anodizing process. *Adv. Mat. Res.* **2011**, *173*, 55–60. [[CrossRef](#)]
38. Kao, T.T.; Chang, Y.C. Influence of anodization parameters on the volume expansion of anodic aluminum oxide formed in mixed solution of phosphoric and oxalic acids. *Appl. Surf. Sci.* **2014**, *288*, 654–659. [[CrossRef](#)]
39. Famiyeh, L.; Huang, X. Plasma electrolytic oxidation coatings on aluminum alloys: Microstructures, properties, and applications. *Mod. Concepts Mater. Sci.* **2019**, *2*, 000526.
40. Bousser, E.; Rogov, A.; Shashkov, P.; Gholinia, A.; Laugel, N.; Slater, T.J.; Withers, P.J.; Matthews, A.; Yerokhin, A. Phase transitions in alumina films during post-sparking anodising of Al alloys. *Acta Mater.* **2023**, *244*, 118587. [[CrossRef](#)]
41. Ismail, R.A.; Zaidan, S.A.; Kadhim, R.M. Preparation and characterization of aluminum oxide nanoparticles by laser ablation in liquid as passivating and anti-reflection coating for silicon photodiodes. *Appl. Nanosci.* **2017**, *7*, 477–487. [[CrossRef](#)]
42. Jing, X.; Zhai, Q.; Zheng, S.; Zhang, D.; Qi, H.; Zhang, D. Surface modification and effects on tribology by laser texturing in  $\text{Al}_2\text{O}_3$ . *Appl. Opt.* **2021**, *60*, 9696–9705. [[CrossRef](#)] [[PubMed](#)]
43. Li, S.; Liu, C. Preparation of the wear and corrosion-resistant coating using a composite process of laser surface texturing technology and plasma electrolytic oxidation. *AIP Adv.* **2023**, *13*, 035204. [[CrossRef](#)]
44. Ito, A.; Kadokura, H.; Kimura, T.; Goto, T. Texture and orientation characteristics of  $\alpha$ - $\text{Al}_2\text{O}_3$  films prepared by laser chemical vapor deposition using Nd: YAG laser. *J. Alloys Compd.* **2010**, *489*, 469–474. [[CrossRef](#)]
45. You, Y.; Ito, A.; Goto, T. Highly (001)-oriented  $\alpha$ - $\text{Al}_2\text{O}_3$  films prepared by laser chemical vapor deposition. *Mater. Lett.* **2013**, *106*, 11–13. [[CrossRef](#)]
46. Zhang, X.; Zhu, J.; Zhang, L.; Han, J.; Du, S. Low-temperature crystallization and hardness enhancement of alumina films using the resputtering technique. *J. Non-Cryst. Solids* **2013**, *362*, 34–39. [[CrossRef](#)]
47. Choy, K.L. Chemical vapour deposition of coatings. *Prog. Mater. Sci.* **2003**, *48*, 57–170. [[CrossRef](#)]
48. Li, W.; Yang, Y.; Liang, H.E.; Zhang, X.; Wang, Y.W.; Gou, J.F. Ablation resistance and mechanism of niobium carbide coatings fabricated by plasma spraying. *Surf. Coat. Technol.* **2023**, *472*, 129934. [[CrossRef](#)]
49. Singh, G.; Vohra, H.; Kaur, M. Fabrication and Characterization of Aluminium Matrix Composites by High Velocity Oxy-Fuel Thermal Spraying. *Adv. Mater. Res.* **2012**, *585*, 317–321. [[CrossRef](#)]

50. Jia, S.K.; Yong, Z.O.U.; Xu, J.Y.; Jing, W.A.N.G.; Lei, Y.U. Effect of TiO<sub>2</sub> content on properties of Al<sub>2</sub>O<sub>3</sub> thermal barrier coatings by plasma spraying. *Trans. Nonferrous Met. Soc. China* **2015**, *25*, 175–183. [[CrossRef](#)]
51. Khorrami, S.A.; Ahmad, M.B.; Lotfi, R.; Shameli, K.; Sedaghat, S.; Shabanzadeh, P.; Baghchesara, M.A. Preparation of  $\gamma$ -Al<sub>2</sub>O<sub>3</sub> nanocrystallites by sol-gel auto combustion process and production of Al-Al<sub>2</sub>O<sub>3</sub> aluminum matrix composites. *Dig. J. Nanomater. Biostructures* **2012**, *7*, 871–876.
52. Korzekwa, J. Modification of the structure and properties of oxide layers on aluminium alloys: A review. *Rev. Adv. Mater. Sci.* **2023**, *62*, 20230108. [[CrossRef](#)]
53. Elkilany, H.A.; Shoeib, M.A.; Abdel-Salam, O.E. Influence of hard anodizing on the mechanical and corrosion properties of different aluminum alloys. *Metallogr. Microstruct. Anal.* **2019**, *8*, 861–870. [[CrossRef](#)]
54. Ali, H.O. Review of porous anodic aluminium oxide (AAO) applications for sensors, MEMS and biomedical devices. *Transactions of the IMF* **2017**, *95*, 290–296. [[CrossRef](#)]
55. Yao, M.; Chen, J.; Yang, P.; Shan, W.; Hu, B.; Yao, X. Preparation and breakdown property of aluminum oxide thin films deposited onto anodized aluminum substrate. *Ferroelectrics* **2013**, *455*, 21–28. [[CrossRef](#)]
56. Brudzisz, A.M.; Giziński, D.; Stępniewski, W.J. Incorporation of ions into nanostructured anodic oxides—Mechanism and functionalities. *Molecules* **2021**, *26*, 6378. [[CrossRef](#)] [[PubMed](#)]
57. Choudhari, K.S.; Choi, C.H.; Chidangil, S.; George, S.D. Recent progress in the fabrication and optical properties of nanoporous anodic alumina. *Nanomaterials* **2022**, *12*, 444. [[CrossRef](#)]
58. Javidi, M.; Fadaee, H. Plasma electrolytic oxidation of 2024-T3 aluminum alloy and investigation on microstructure and wear behavior. *Appl. Surf. Sci.* **2013**, *286*, 212–219. [[CrossRef](#)]
59. Dunleavy, C.S.; Golosnoy, I.O.; Curran, J.A.; Clyne, T.W. Characterisation of discharge events during plasma electrolytic oxidation. *Surf. Coat. Technol.* **2009**, *203*, 3410–3419. [[CrossRef](#)]
60. Fernández-López, P.; Alves, S.A.; San-Jose, J.T.; Gutierrez-Berasategui, E.; Bayón, R. Plasma Electrolytic Oxidation (PEO) as a Promising Technology for the Development of High-Performance Coatings on Cast Al-Si Alloys: A Review. *Coatings* **2024**, *14*, 217. [[CrossRef](#)]
61. Sikdar, S.; Menezes, P.V.; Maccione, R.; Jacob, T.; Menezes, P.L. Plasma electrolytic oxidation (PEO) process—Processing, properties, and applications. *Nanomaterials* **2021**, *11*, 1375. [[CrossRef](#)]
62. Hussein, R.O.; Nie, X.; Northwood, D.O. An investigation of ceramic coating growth mechanisms in plasma electrolytic oxidation (PEO) processing. *Electrochim. Acta* **2013**, *112*, 111–119. [[CrossRef](#)]
63. Wang, S.; Liu, X.; Yin, X.; Du, N. Influence of electrolyte components on the microstructure and growth mechanism of plasma electrolytic oxidation coatings on 1060 aluminum alloy. *Surf. Coat. Technol.* **2020**, *381*, 125214. [[CrossRef](#)]
64. Nsilani Kouediatouka, A.; Ma, Q.; Liu, Q.; Mawignon, F.J.; Rafique, F.; Dong, G. Design methodology and application of surface texture: A review. *Coatings* **2022**, *12*, 1015. [[CrossRef](#)]
65. Kromer, R.; Costil, S.; Cormier, J.; Courapied, D.; Berthe, L.; Peyre, P.; Boustie, M. Laser surface patterning to enhance adhesion of plasma sprayed coatings. *Surf. Coat. Technol.* **2015**, *278*, 171–182. [[CrossRef](#)]
66. Cao, Q.; Wang, Z.; He, W.; Guan, Y. Fabrication of super hydrophilic surface on alumina ceramic by ultrafast laser microprocessing. *Appl. Surf. Sci.* **2021**, *557*, 149842. [[CrossRef](#)]
67. Sciancalepore, C.; Gemini, L.; Romoli, L.; Bondioli, F. Study of the wettability behavior of stainless steel surfaces after ultrafast laser texturing. *Surf. Coat. Technol.* **2018**, *352*, 370–377. [[CrossRef](#)]
68. Shaikh, S.; Kedia, S.; Singh, D.; Subramanian, M.; Sinha, S. Surface texturing of Ti6Al4V alloy using femtosecond laser for superior antibacterial performance. *J. Laser Appl.* **2019**, *31*, 022011. [[CrossRef](#)]
69. Tomanik, M.; Kobielarz, M.; Filipiak, J.; Szymonowicz, M.; Rusak, A.; Mroczkowska, K.; Antończak, A.; Pezowicz, C. Laser texturing as a way of influencing the micromechanical and biological properties of the poly (L-lactide) surface. *Materials* **2020**, *13*, 3786. [[CrossRef](#)]
70. Yang, C.; Jing, X.; Wang, F.; Ehmman, K.F.; Tian, Y.; Pu, Z. Fabrication of controllable wettability of crystalline silicon surfaces by laser surface texturing and silanization. *Appl. Surf. Sci.* **2019**, *497*, 143805. [[CrossRef](#)]
71. Etsion, I. Improving tribological performance of mechanical components by laser surface texturing. *Tribol. Lett.* **2004**, *17*, 733–737. [[CrossRef](#)]
72. Mao, B.; Siddaiah, A.; Liao, Y.; Menezes, P.L. Laser surface texturing and related techniques for enhancing tribological performance of engineering materials: A review. *J. Manuf. Process.* **2020**, *53*, 153–173. [[CrossRef](#)]
73. Gachot, C.; Rosenkranz, A.; Hsu, S.M.; Costa, H.L. A critical assessment of surface texturing for friction and wear improvement. *Wear* **2017**, *372*, 21–41. [[CrossRef](#)]
74. Ferreira, R.; Carvalho, Ó.; Sobral, L.; Carvalho, S.; Silva, F. Laser texturing of piston ring for tribological performance improvement. *Friction* **2023**, *11*, 1895–1905. [[CrossRef](#)]
75. Shamsul Baharin, A.F.; Ghazali, M.J.; Wahab, A.J. Laser surface texturing and its contribution to friction and wear reduction: A brief review. *Ind. Lubr. Tribol.* **2016**, *68*, 57–66. [[CrossRef](#)]
76. Cao, L.; Chen, Y.; Cui, J.; Li, W.; Lin, Z.; Zhang, P. Corrosion wear performance of pure titanium laser texturing surface by nitrogen ion implantation. *Metals* **2020**, *10*, 990. [[CrossRef](#)]
77. Fan, Y.; Xu, L.; Liu, S.; Li, J.; Xia, J.; Qin, X.; Li, Y.; Gao, T.; Tang, X. The state-of-the-art and perspectives of laser ablation for tumor treatment. *Cyborg Bionic Syst.* **2024**, *5*, 0062. [[CrossRef](#)] [[PubMed](#)]



78. Holá, M.; Ondráček, J.; Nováková, H.; Vojtíšek-Lom, M.; Hadravová, R.; Kanický, V. The influence of material properties on highly time resolved particle formation for nanosecond laser ablation. *Acta B At. Spectrosc.* **2018**, *148*, 193–204. [[CrossRef](#)]
79. John, M.; Ralls, A.M.; Kuruveri, U.B.; Menezes, P.L. Tribological, corrosion, and microstructural features of laser-shock-peened steels. *Metals* **2023**, *13*, 397. [[CrossRef](#)]
80. Gu, C.; Tian, Z.; Zhao, J.; Wang, Y. Investigation of microstructure and tribological property of Ti-6Al-4V alloy by laser shock peening processing. *Int. J. Adv. Manuf. Technol.* **2023**, *129*, 955–967. [[CrossRef](#)]
81. Shukla, P.; Crookes, R.; Wu, H. Shock-wave induced compressive stress on alumina ceramics by laser peening. *Mater. Des.* **2019**, *167*, 107626. [[CrossRef](#)]
82. Wang, F.; Zhang, C.; Lu, Y.; Nastasi, M.; Cui, B. Laser shock processing of polycrystalline alumina ceramics. *J. Am. Ceram. Soc.* **2017**, *100*, 911–919. [[CrossRef](#)]
83. Sathyaseelan, B.; Baskaran, I.; Sivakumar, K. Phase transition behavior of nanocrystalline Al<sub>2</sub>O<sub>3</sub> powders. *Soft Nanosci. Lett.* **2013**, *3*, 69–74. [[CrossRef](#)]
84. Matori, K.A.; Wah, L.C.; Hashim, M.; Ismail, I.; Zaid, M.H.M. Phase transformations of  $\alpha$ -alumina made from waste aluminum via a precipitation technique. *Int. J. Mol. Sci.* **2012**, *13*, 16812–16821. [[CrossRef](#)] [[PubMed](#)]
85. Palmero, P.; Lombardi, M.; Montanaro, L.; Azar, M.; Chevalier, J.; Garnier, V.; Fantozzi, G. Effect of heating rate on phase and microstructural evolution during pressureless sintering of a nanostructured transition alumina. *Int. J. Appl. Ceram. Technol.* **2009**, *6*, 420–430. [[CrossRef](#)]
86. Mahat, A.M.; Mastuli, M.S.; Kamarulzaman, N. Influence of annealing temperature on the phase transformation of Al<sub>2</sub>O<sub>3</sub>. *AIP Conf. Proc.* **2016**, *1711*, 050001.
87. Zhou, J.; Liao, C.; Shen, H.; Ding, X. Surface and property characterization of laser polished Ti<sub>6</sub>Al<sub>4</sub>V. *Surf. Coat. Technol.* **2019**, *380*, 125016. [[CrossRef](#)]
88. Moura, C.G.; Carvalho, O.; Gonçalves, L.M.V.; Cerqueira, M.F.; Nascimento, R.; Silva, F. Laser surface texturing of Ti-6Al-4V by nanosecond laser: Surface characterization, Ti-oxide layer analysis and its electrical insulation performance. *Mater. Sci. Eng. C* **2019**, *104*, 109901. [[CrossRef](#)] [[PubMed](#)]
89. Chen, L.; Ren, X.; Zhou, W.; Tong, Z.; Adu-Gyamfi, S.; Ye, Y.; Ren, Y. Evolution of microstructure and grain refinement mechanism of pure nickel induced by laser shock peening. *Mater. Sci. Eng. A* **2018**, *728*, 20–29. [[CrossRef](#)]
90. Wang, H.; Lin, H.; Wang, C.; Zheng, L.; Hu, X. Laser drilling of structural ceramics—A review. *J. Eur. Ceram. Soc.* **2017**, *37*, 1157–1173. [[CrossRef](#)]
91. Li, Z.; Li, B.Q.; Bai, P.; Liu, B.; Wang, Y. Research on the thermal behaviour of a selectively laser melted aluminium alloy: Simulation and experiment. *Materials* **2018**, *11*, 1172. [[CrossRef](#)] [[PubMed](#)]
92. Byskov-Nielsen, J. Short-Pulse Laser Ablation of Metals: Fundamentals and Applications for Micro-Mechanical Interlocking. Doctoral Dissertation, Department of Physics and Astronomy, University of Aarhus, Aarhus, Denmark, 2010.
93. Zhao, W.; Mei, X.; Yang, Z. Simulation and experimental study on group hole laser ablation on Al<sub>2</sub>O<sub>3</sub> ceramics. *Ceram. Int.* **2022**, *48*, 4474–4483. [[CrossRef](#)]
94. Farshidianfar, M.H.; Khajepour, A.; Gerlich, A.P. Effect of real-time cooling rate on microstructure in laser additive manufacturing. *J. Mater. Process. Technol.* **2016**, *231*, 468–478. [[CrossRef](#)]
95. Furushima, Y.; Schick, C.; Toda, A. Crystallization, recrystallization, and melting of polymer crystals on heating and cooling examined with fast scanning calorimetry. *Polym. Cryst.* **2018**, *1*, e10005. [[CrossRef](#)]
96. Lee, D.; Zhao, B.; Perim, E.; Zhang, H.; Gong, P.; Gao, Y.; Liu, Y.; Toher, C.; Curtarolo, S.; Schroers, J.; et al. Crystallization behavior upon heating and cooling in Cu<sub>50</sub>Zr<sub>50</sub> metallic glass thin films. *Acta Mater.* **2016**, *121*, 68–77. [[CrossRef](#)]
97. Ibrahim, A.; Hung, Y. Laser Surface Annealing of Plasma Sprayed Coatings. *J. Surf. Eng. Mater. Adv. Technol.* **2012**, *2*, 215–220. [[CrossRef](#)]
98. Moriya, R.; Iguchi, M.; Sasaki, S.; Yan, J. Surface property modification of alumina sprayed coatings using Nd: YAG laser. *Procedia CIRP* **2016**, *42*, 464–469. [[CrossRef](#)]

**Disclaimer/Publisher's Note:** The statements, opinions and data contained in all publications are solely those of the individual author(s) and contributor(s) and not of MDPI and/or the editor(s). MDPI and/or the editor(s) disclaim responsibility for any injury to people or property resulting from any ideas, methods, instructions or products referred to in the content.